The Astrophysical Journal, 944:98 (9pp), 2023 February 10 https://doi.org/10.3847/1538-4357/acb33b

Observations of Waves and Structures by Frequency–Wavenumber Spectrum in Solar Wind Turbulence

L.-L. Zhao[1,2], G. P. Zank[1,2], M. Nakanotani[1,2], and L. Adhikari[1,2]
[1] Center for Space Plasma and Aeronomic Research (CSPAR), The University of Alabama in Huntsville, Huntsville, AL 35805, USA; lz0009@uah.edu
[2] Department of Space Science, The University of Alabama in Huntsville, Huntsville, AL 35805, USA
Received 2022 October 13; revised 2023 January 12; accepted 2023 January 12; published 2023 February 15

Abstract

A well-known shortcoming of single-spacecraft spectral analysis is that only the 1D wavenumber spectrum can be observed, assuming the characteristic wave propagation speed is much smaller than the solar wind flow speed. This limitation has motivated an extended debate about whether fluctuations observed in the solar wind are waves or structures. Multispacecraft analysis techniques can be used to calculate the wavevector independent of the observed frequency, thus allowing one to study the frequency–wavenumber spectrum of turbulence directly. The dispersion relation for waves can be identified, which distinguishes them from nonpropagating structures. We use magnetic field data from the four Magnetospheric Multiscale (MMS) spacecraft to measure the frequency–wavenumber spectrum of solar wind turbulence based on the *k*-filtering and phase differencing techniques. Both techniques have been used successfully in the past for the Earth's magnetosphere, although applications to solar wind turbulence have been limited. We conclude that the solar wind turbulence intervals observed by MMS show features of nonpropagating structures that are associated with frequencies close to zero in the plasma rest frame. However, there is no clear evidence of propagating Alfvén waves that have a nonzero rest-frame frequency. The lack of waves may be due to instrument noise and spacecraft separation. Our results support the idea of turbulence dominated by quasi-2D structures.

Unified Astronomy Thesaurus concepts: Solar wind (1534); Interplanetary turbulence (830)

1. Introduction

Whether solar wind turbulence is composed of propagating waves or nonlinear structures has been debated extensively. It is well known that the linearized magnetohydrodynamic (MHD) equations yield Alfvén, fast magnetosonic, and slow magnetosonic modes. In the solar wind, turbulence is weakly compressible and typically possesses Alfvénic signatures in the form of highly correlated (or anticorrelated) velocity and magnetic fluctuations (Belcher & Davis 1971). However, because of the limitation of single-spacecraft observations, it cannot be determined unambiguously whether turbulence is indeed composed of propagating waves. Solar wind observations typically assume that Taylor's hypothesis holds, meaning that temporal variations are interpreted as spatial structures so that the wave dispersion relations cannot be verified (e.g., Matthaeus et al. 2016). Nevertheless, many previous works have investigated the properties of turbulence based on the linear wave assumption both theoretically and observationally. The linear wave eigenmodes of MHD have been used as the basis set to decompose any observed velocity, magnetic field, and density fluctuations into linear waves (Glassmeier et al. 1995; Cho & Lazarian 2003). This approach has been widely used in many recent observations in an attempt to identify constituent MHD waves in the solar wind (Chaston et al. 2020; Zhu et al. 2020; Zhao et al. 2021, 2022).

While multispacecraft methods have been developed for decades, their application to the spectral analysis of solar wind turbulence has been rare. Most observations using multiple spacecraft address turbulence and waves in the terrestrial magnetosheath (e.g., Narita et al. 2016; Roberts et al. 2019; He et al. 2020; Lin et al. 2022). In studying solar wind turbulence, Sahraoui et al. (2010b) used Cluster spacecraft data to construct 3D dispersion relations, from which they concluded that the turbulence cascade at the subproton scale is due to kinetic Alfvén waves propagating perpendicularly to the mean magnetic field. Recently, Zhao et al. (2022) provided evidence of propagating MHD-scale Alfvén waves using MMS spacecraft. Frequency–wavenumber spectra were obtained using a multispacecraft timing analysis and the incompressible component of the magnetic fluctuations is shown to be consistent with the linear Alfvén wave dispersion relation. However, it should be noted that Zhao et al. (2022) consider the frequency–wavenumber spectrum subject to the assumption that the perpendicular wavevector $k_\perp = 0$. This raises the possibility that even if Alfvén waves are present, the region in *k*-space near $k_\perp = 0$ might also contain a significant amount of power, in the form of quasi-2D fluctuations (e.g., Matthaeus et al. 1990; Zank & Matthaeus 1993; Bieber et al. 1996; Zank et al. 2017). Therefore, an analysis that considers both the Alfvénic and quasi-2D regions is needed. In this paper, we revisit the solar wind burst mode intervals observed by the MMS mission (Roberts et al. 2020) using both *k*-filtering and phase differencing methods. We present the frequency–wavenumber power spectra of the magnetic field fluctuations. The goal is to address the zero-frequency part of the solar wind turbulence spectrum that has usually been neglected in previous studies.

2. Methodology

We use two multispacecraft spectral analysis methods in this paper, namely *k*-filtering and phase differencing. The derivation and detailed procedure of *k*-filtering can be found in

Pincon & Lefeuvre (1988), Motschmann et al. (1996), Pincon & Motschmann (1998) and is not repeated here. A discussion of the applicability and uncertainties of the method is discussed in Sahraoui et al. (2010a). The product of k-filtering is an estimate of the 4D frequency–wavenumber spectrum $P(\omega, \boldsymbol{k})$, assuming time stationarity and spatial homogeneity. For magnetic field data measured with four spacecraft $\boldsymbol{B}(\boldsymbol{r}_i)$, $i = 1,\ldots,4$, the result is given by

$$P(\omega, \boldsymbol{k}) = Tr\{[H^{\dagger}(\boldsymbol{k})M^{-1}(\omega)H(\boldsymbol{k})]^{-1}\}. \quad (1)$$

Here, † represents the conjugate transpose. The matrix H is constructed as a 12×3 matrix

$$H = \begin{pmatrix} Ie^{-i\boldsymbol{k}\cdot\boldsymbol{r}_1} \\ Ie^{-i\boldsymbol{k}\cdot\boldsymbol{r}_2} \\ Ie^{-i\boldsymbol{k}\cdot\boldsymbol{r}_3} \\ Ie^{-i\boldsymbol{k}\cdot\boldsymbol{r}_4} \end{pmatrix}, \quad (2)$$

where I is a 3×3 identity matrix. The matrix M is calculated as

$$M = \frac{1}{N}\sum_i A_i(\omega)A_i^{\dagger}(\omega), \quad (3)$$

which is an average over N subintervals. The 12×1 matrix A for each subinterval is constructed from the Fourier transform of the magnetic field measured by the four spacecraft,

$$A = \begin{pmatrix} \tilde{\boldsymbol{B}}(\omega, \boldsymbol{r}_1) \\ \tilde{\boldsymbol{B}}(\omega, \boldsymbol{r}_2) \\ \tilde{\boldsymbol{B}}(\omega, \boldsymbol{r}_3) \\ \tilde{\boldsymbol{B}}(\omega, \boldsymbol{r}_4) \end{pmatrix}. \quad (4)$$

The k-filtering method has been used frequently with Cluster spacecraft in the magnetosheath and near discontinuities (e.g., Sahraoui et al. 2006; Efthymiadis et al. 2007; Narita et al. 2010).

Phase differencing is another method, which is based on the phase difference of waves at different spacecraft locations (Balikhin et al. 2003). It is useful when there is a dominant mode at each observed frequency. The wavevector at a certain frequency is related to the phase difference between two spacecraft by

$$\boldsymbol{k} \cdot \Delta\boldsymbol{r} = \Delta\phi, \quad (5)$$

which gives the projection of the wavevector along the direction of spacecraft separation. Given four spacecraft measurements, the full wavevector can be determined by solving

$$\begin{pmatrix} \boldsymbol{r}_1^T - \boldsymbol{r}_2^T \\ \boldsymbol{r}_1^T - \boldsymbol{r}_3^T \\ \boldsymbol{r}_1^T - \boldsymbol{r}_4^T \end{pmatrix}\boldsymbol{k} = \begin{pmatrix} \Phi_2 - \Phi_1 \\ \Phi_3 - \Phi_1 \\ \Phi_4 - \Phi_1 \end{pmatrix}, \quad (6)$$

with $\boldsymbol{r}$ and $\boldsymbol{k}$ being column vectors. The power $P(\omega, \boldsymbol{k})$ can then be calculated as the average Fourier power among four spacecraft. Walker et al. (2004) compare the phase differencing and k-filtering methods, and the basic results from the two methods are consistent with each other. The k-filtering method is slightly more advantageous because it can identify the dispersion of more than one mode. For example, Walker et al. (2004) show that both the nonpropagating mirror mode and Alfvén-like cyclotron waves can be identified by the k-filtering method. It is critical to consider the range of wavevectors for which these two techniques are applicable. In general, the maximum wavenumber $k_{\max}$ applicable to both methods is given by $\pi/d_{\rm av}$, where $d_{\rm av}$ is the average separation of the spacecraft. This is because fluctuations in k-space separated by $2n\pi/d_{\rm av}$ cannot be distinguished due to aliasing effects (Lin et al. 2022). For the determination of $k_{\min}$, we use the empirical estimate provided by Sahraoui et al. (2010a), which shows that the uncertainty increases significantly when the wavenumber is close to or less than $k_{\min} \sim 0.01k_{\max}$.

In this study, we use mean-field coordinates where the mean magnetic field $\boldsymbol{B}_0$ is along the z-axis; the y-axis is perpendicular to both the mean magnetic field and the mean flow velocity, i.e., $\boldsymbol{y} \propto \boldsymbol{B}_0 \times \boldsymbol{V}_{\rm sw}$; and the x-direction completes a right-handed triad. The four MMS spacecraft magnetic field measurements and the location separation $\Delta\boldsymbol{r}$ are transformed into the mean-field coordinates. For the k-filtering method, we use all three magnetic field components to maximize the available information (Tjulin et al. 2005). For the phase differencing method, we use only the B_y component in the mean-field coordinates, which is the component perpendicular to the mean magnetic field and the mean flow speed, corresponding to incompressible Alfvén waves and quasi-2D structures.

For the mean-field $\boldsymbol{B}_0$ calculation, we use the global mean field averaged over the entire interval, which is both scale (or frequency) and time independent. We do not think this greatly affects our results. The use of a scale-dependent mean field (e.g., Podesta 2009) affects the more subtle analysis of the anisotropic scaling of the power spectrum or structure function, which is beyond the scope of our current analysis. Our present work simply focuses on the identification of waves and advected structures through dispersion relations. The calculation of the mean magnetic field is expected to have little effect on the results presented below.

3. Data Overview and Results

For data selection, we use MMS solar wind burst mode intervals as in Roberts et al. (2020). We consider two intervals in this study, 21:09:43–21:48:47 on 2017 November 26 and 14:40:03–15:08:24 on 2017 December 18. As shown in Figure 1, the MMS spacecraft (red dot) is located beyond the Earth's magnetopause (yellow curve) and bow shock (blue curve) during both intervals. Specifically, the first interval (left panel) is located at approximately $[17.3, 16.8, 6.3]R_E$, and the second interval is about $[16.3, 2.0, 3.4]R_E$ in the geocentric solar ecliptic (GSE) coordinates. Both intervals can be used to study fluctuations in the solar wind plasma. We note that the bow shock could have some influence on the observation because the data intervals may not be in the pristine solar wind. For the first interval shown on the left panel, we find that the spacecraft are relatively far away from the shock, and the solar wind magnetic field is close to perpendicular to the shock normal at the nose, indicating that the data are likely not highly influenced by the bow shock. On the other hand, the second interval shown on the right panel is more likely to be affected by the bow shock since the magnetic field is oblique and the spacecraft are close to the nose. Nevertheless, the basic results presented below are similar for both intervals, and we do not quantify the influence of bow shock in this study.

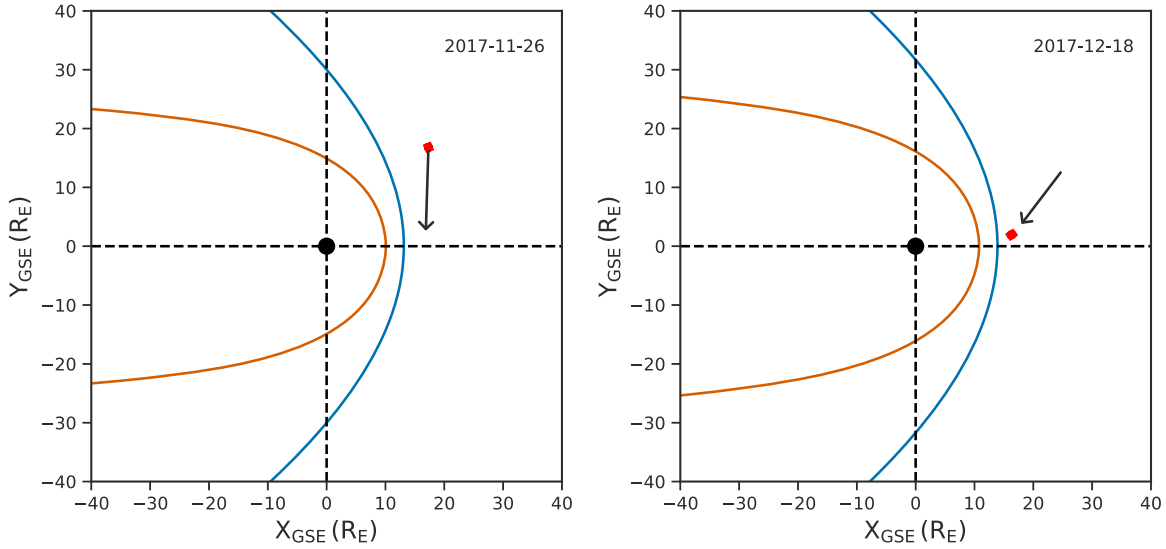

Figure 1. Projection of the location of the MMS (red dot) in the selected intervals onto the *X*-*Y* plane of the GSE coordinate system. The blue and yellow curves represent experimental models of the Earth's bow shock (Farris & Russell 1994) and magnetopause (Shue et al. 1998), respectively, and are calculated using OMNI solar wind measurements in each interval. The black arrow indicates the direction of the background mean magnetic field in each interval.

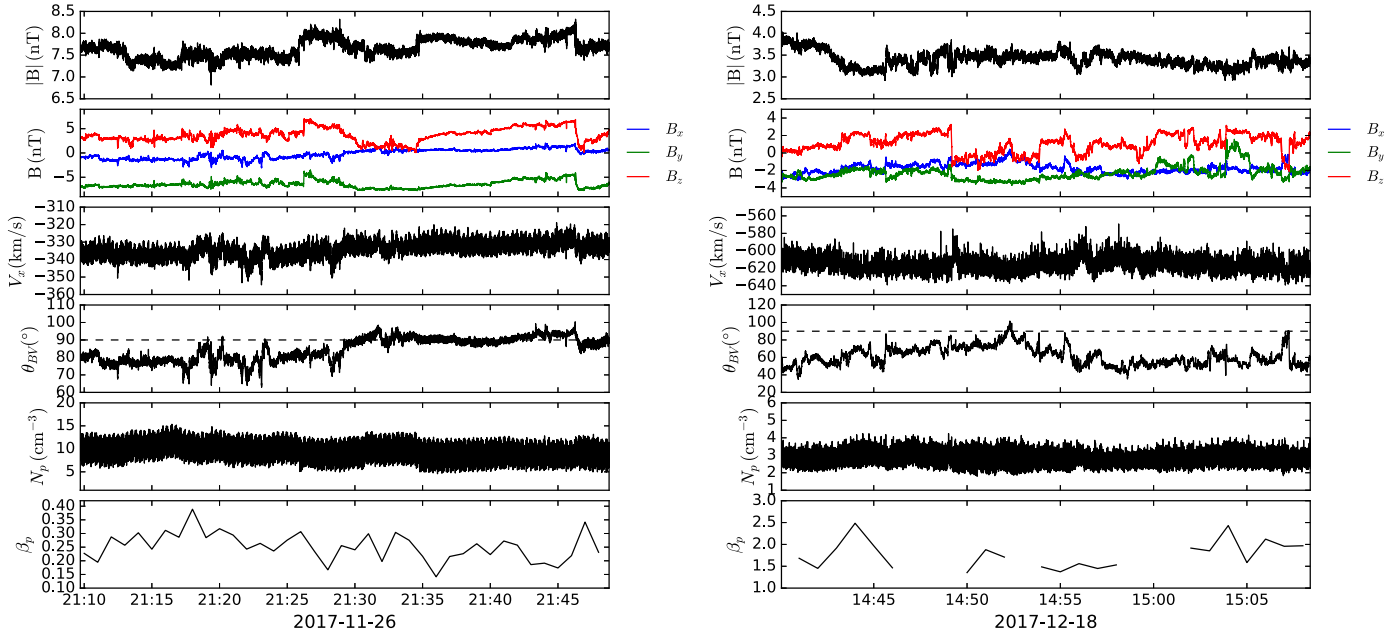

Figure 2. An overview of the solar wind parameters observed by MMS1. The left panel is for the selected solar wind interval during 21:09–21:48 on 2017 November 26. The right panel shows another solar wind interval during 14:40–15:08 on 2017 December 18. The panels from top to bottom show the magnetic field magnitude $|B|$ and its components, plasma radial speed V_x, the angle between the magnetic field and velocity field θ_{BV}, proton density N_p, and the proton plasma beta β_p. Proton temperature measurements from OMNI are used in the calculation of β_p.

Figure 2 provides an overview of the magnetic field and solar wind plasma measured by MMS1 during the selected intervals on 2017 November 26 (left panel) and 2017 December 18 (right panel), respectively. We use the magnetic field measurements in burst mode with a sampling rate of 128 Hz from the fluxgate magnetometers (FGMs; Russell et al. 2016) onboard the four MMS spacecraft. The proton plasma measurements, including speed and density with a sampling rate of 6.6 Hz, are obtained from the Fast Plasma Investigation (FPI; Pollock et al. 2016) onboard MMS1. Due to the limitations of FPI in the solar wind plasma (Bandyopadhyay et al. 2018), we use the proton temperature data time-shifted to the nose of the Earth's bow shock provided by OMNI (King & Papitashvili 2005) when calculating the proton plasma beta.

As shown in Figure 2, Interval 1 on 2017 November 26 is characterized by a slow solar wind stream with an average velocity vector $\boldsymbol{V}_{sw}$ of $[-334, -11, 22]$ km s^{-1} in GSE coordinates. The relative magnetic field fluctuation amplitude $\delta B/B_0$ observed by MMS1 is about 0.25, and is simply calculated from the standard deviation of the magnetic field (which includes fluctuations at all scales) divided by the mean magnetic field magnitude of the interval. We do not consider its scale dependence in this analysis. The angle θ_{BV} is close to 90°, indicating that the magnetic field and velocity field are approximately perpendicular to each other in this interval.

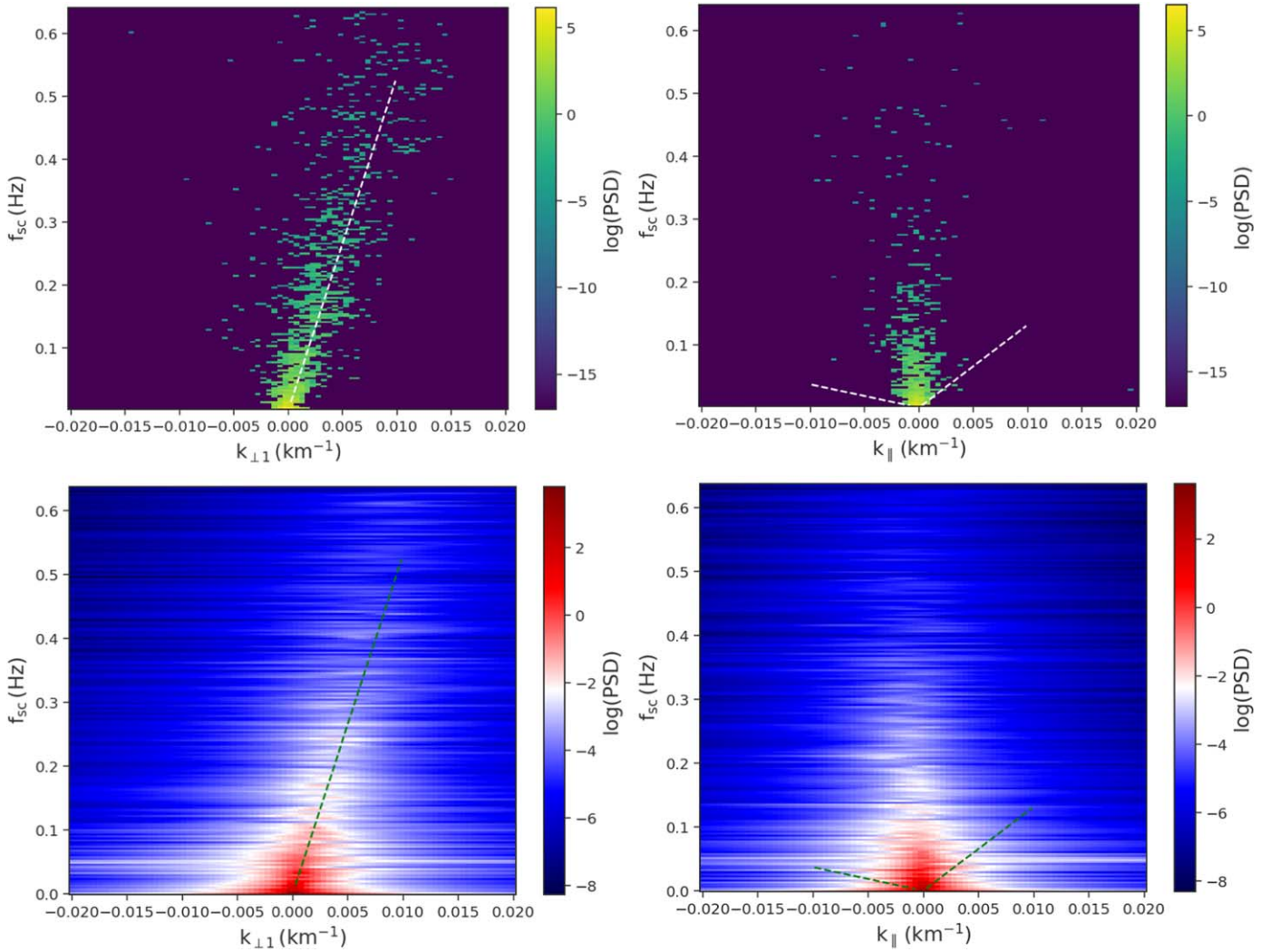

Figure 3. Frequency–wavenumber (ω–$\boldsymbol{k}$) power spectrum density (PSD) for the solar wind interval on 2017 November 26 using the phase differencing method (top two panels) and k-filtering method (bottom two panels) for perpendicular $k_{\perp 1}$ or k_x (left panels) and parallel $k_\parallel$ (right panels) wavenumbers, respectively. The dashed lines in the left and right panels illustrate the dispersion relations for the nonpropagating advected structures and propagating Alfvén waves, respectively.

Table 1
List of Parameters in the MMS Solar Wind Intervals

Date	Start Time UT	End Time UT	$\lvert B\rvert$ nT	$\lvert V_{\rm sw}\rvert$ km s^{-1}	N_p cm^{-3}	T_p 10^5 K	$V_{\rm A}$ km s^{-1}	$d_{\rm i}$ km	$\rho_{\rm i}$ km	β_p
2017/11/26	21:09:43	21:48:47	7.7	335	9.4	0.45	54	74	26	0.25
2017/12/18	14:40:03	15:08:24	3.4	616	2.8	2.0	44	136	126	1.77

Note. T_p is the proton temperature measured by OMNI, $V_{\rm A}$ is the Alfvén speed, d_i is the ion inertial length, and ρ_i is the thermal proton gyroradius.

Interval 2, on 2017 December 18, features a relatively fast solar wind speed $V_{\rm sw}$ of around 616 km s^{-1} and a more oblique angle θ_{BV}. The mean velocity field during this interval is around $[-615, 36, -13]$ km s^{-1}, and the magnetic field fluctuation amplitude $\delta B/B_0$ is about 0.46. The average values of other solar wind parameters during each interval are listed in Table 1. Here, the proton temperature T_p obtained from OMNI is used to calculate the thermal proton gyroradius ρ_i and plasma beta β_p. As described in Section 2, the solar wind plasma parameters in this study are only required for calculating the average velocity vector and the averaged plasma density. They are used for the mean-field coordinate construction and the calculation of the Alfvén speed, and thus the comparison to the theoretical dispersion relations.

We first show the results from both the phase differencing and k-filtering methods for Interval 1 on 2017 November 26 in Figure 3. The top two panels show the frequency–wavenumber spectrum from the phase differencing method, and the bottom two panels show results from the k-filtering method. We use $k_\parallel$ to denote the wavevector along the z-axis in the mean-field coordinate system, while $k_{\perp 1}$ and $k_{\perp 2}$ denote the wavevector along the x-axis and y-axis of the mean-field coordinate, respectively.

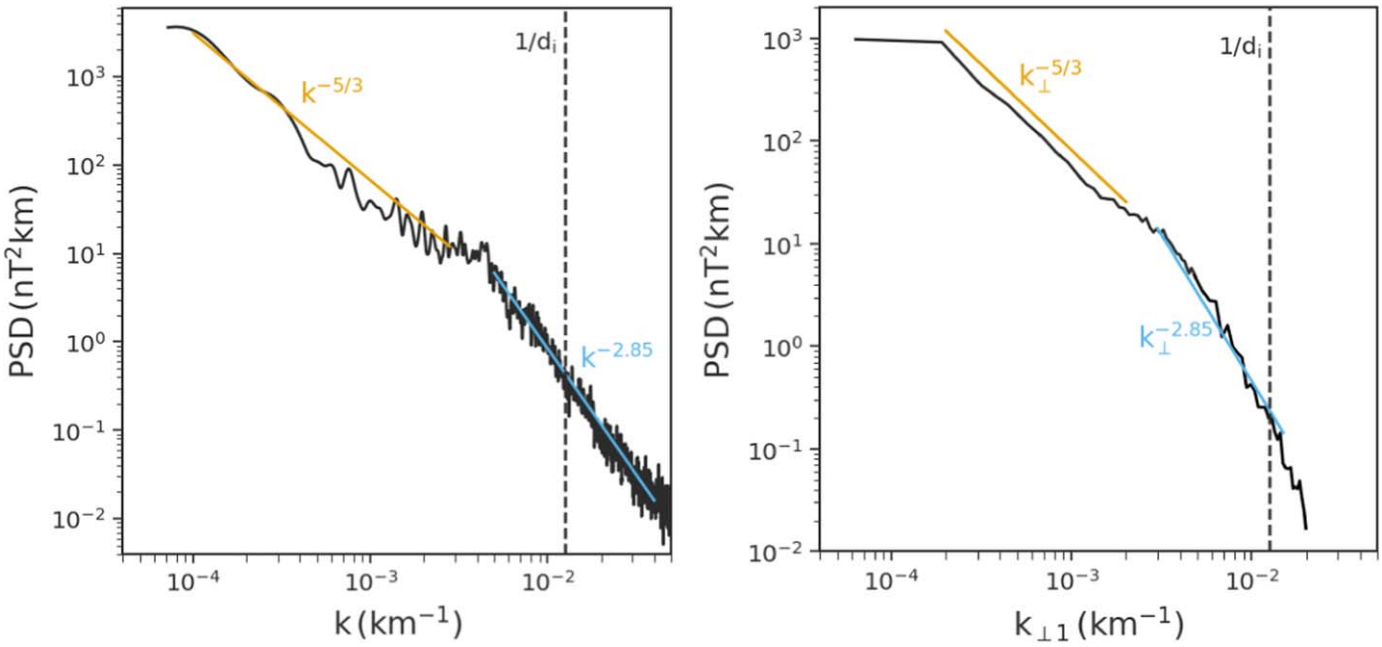

Figure 4. Wavenumber spectra of the magnetic field B_y component for Interval 1 calculated with Taylor's hypothesis (left panel) and the phase differencing method (right panel).

To present the fluctuating magnetic field frequency–wavenumber (ω-$\boldsymbol{k}$) power spectrum density (PSD), we show two cross-sectional cuts of ω-$\boldsymbol{k}$ space, the first with $k_{\parallel} = k_{\perp 2} = 0$ representing the spectrum for the incompressible $\perp 1$ fluctuations (left panels), and the second with $k_{\perp 1} = k_{\perp 2} = 0$ representing the PSD in the parallel direction (right panels). The vertical axes of the figure are the Fourier frequencies observed in the spacecraft frame f_{sc}, related to the circular frequency ω as $\omega = 2\pi f_{\rm sc}$. In all four panels, we see the fluctuation power tends to decrease with increasing frequency. The left panels show that most of the spectral power follows the dispersion relation $\omega = \boldsymbol{k} \cdot \boldsymbol{V}_{\rm sw}$, as demonstrated by the dashed lines. We note that the PSD in the $\perp 2$ direction has the same features (not shown here). This suggests that the fluctuations with perpendicular wavenumbers are dominated by nonpropagating structures advected with the solar wind flow. This is similar to what has been found previously in the Earth's magnetosheath (Chisham et al. 1998; Balikhin et al. 2003; Walker et al. 2004), where it is interpreted as the nonpropagating mirror mode. Since we are considering the incompressible component, and the plasma beta in the solar wind is lower than that of the magnetosheath, we interpret our results as consistent with 2D magnetic island-like structures.

The right panels of Figure 3 show the spectral power in ω-$k_{\parallel}$ space. The two dashed lines in each panel represent the Alfvén wave dispersion relation for wave propagation in two opposite directions. The dispersion relations for counterpropagating Alfvén waves is $\omega = \boldsymbol{k} \cdot \boldsymbol{V}_{\rm sw} \pm k_{\parallel} V_{\rm A}$, respectively. The Figure 3 right panels show no clear evidence of either propagating waves or advected structures. We note that since the mean magnetic field $\boldsymbol{B}_0$ is approximately aligned with the $\perp 1$ (or x-axis in the mean-field coordinate) direction during the interval, the Doppler shift for the observed frequency is small for parallel wavevectors. Our results here are distinctly different from those obtained by Zhao et al. (2022), in which strong signatures of the Alfvén wave dispersion relation were found. We note that the Alfvén speed in the interval is $\sim$50 km s^{-1}, which is much smaller than the solar wind bulk speed of $\sim$330 km s^{-1}. Therefore, the detection of Alfvén waves may need a very fine resolution in frequency to be clearly distinguished from advected structures. The figures suggest that most of the power is concentrated in a region with small $k_{\parallel}$ and large f_{sc} ($f_{\rm sc} \gg |\boldsymbol{k} \cdot \boldsymbol{V}_{\rm sw} \pm k_{\parallel} V_{\rm A}|$), which seems unphysical. We show later that instrument noise may play a significant role in the parallel spectrum.

The results from the k-filtering method for Interval 1 are shown in the bottom two panels of Figure 3. Overall, the results from the two methods are similar. The perpendicular ω-$k_{\perp 1}$ spectrum follows the dispersion relation $\omega = \boldsymbol{k} \cdot \boldsymbol{V}_{\rm sw}$, which is again consistent with nonpropagating advected structures, and the parallel wavevector spectrum does not show clear evidence of propagating Alfvén waves as most of the spectral power lies outside the dispersion relations defined by two counter-propagating Alfvén waves.

Figure 4 shows the wavenumber power spectra of the B_y component in the mean-field coordinates during Interval 1. The left panel shows the spectrum converted from the Fourier frequency spectrum using Taylor's hypothesis ($k = 2\pi\omega/|V_{\rm sw}|$), where the frequency spectrum is calculated by the standard Welch method. The right panel is reduced from the phase differencing method by $P(k_{\perp 1}) = \int P(\omega, \boldsymbol{k}) d\omega dk_{\parallel} dk_{\perp 2}$. The two spectra are consistent with each other and exhibit a broken power-law shape. The inertial-range and dissipation-range spectra are consistent with $k^{-5/3}$ and $k^{-2.85}$, which are shown in the figure as references. The spectral break appears to be at a larger scale (or smaller wavenumber) than the ion inertial length d_i, indicating that dissipation occurs at a larger scale than that defined by d_i.

Consider now Interval 2 on 2017 December 18, which has a less perpendicular flow velocity and a faster solar wind stream. Figure 5 shows the frequency–wavenumber ω-$\boldsymbol{k}$ spectra after using the phase differencing method for Interval 2. The k-filtering results are similar and not shown here. The top two panels show the PSD for larger wavenumbers and frequencies,

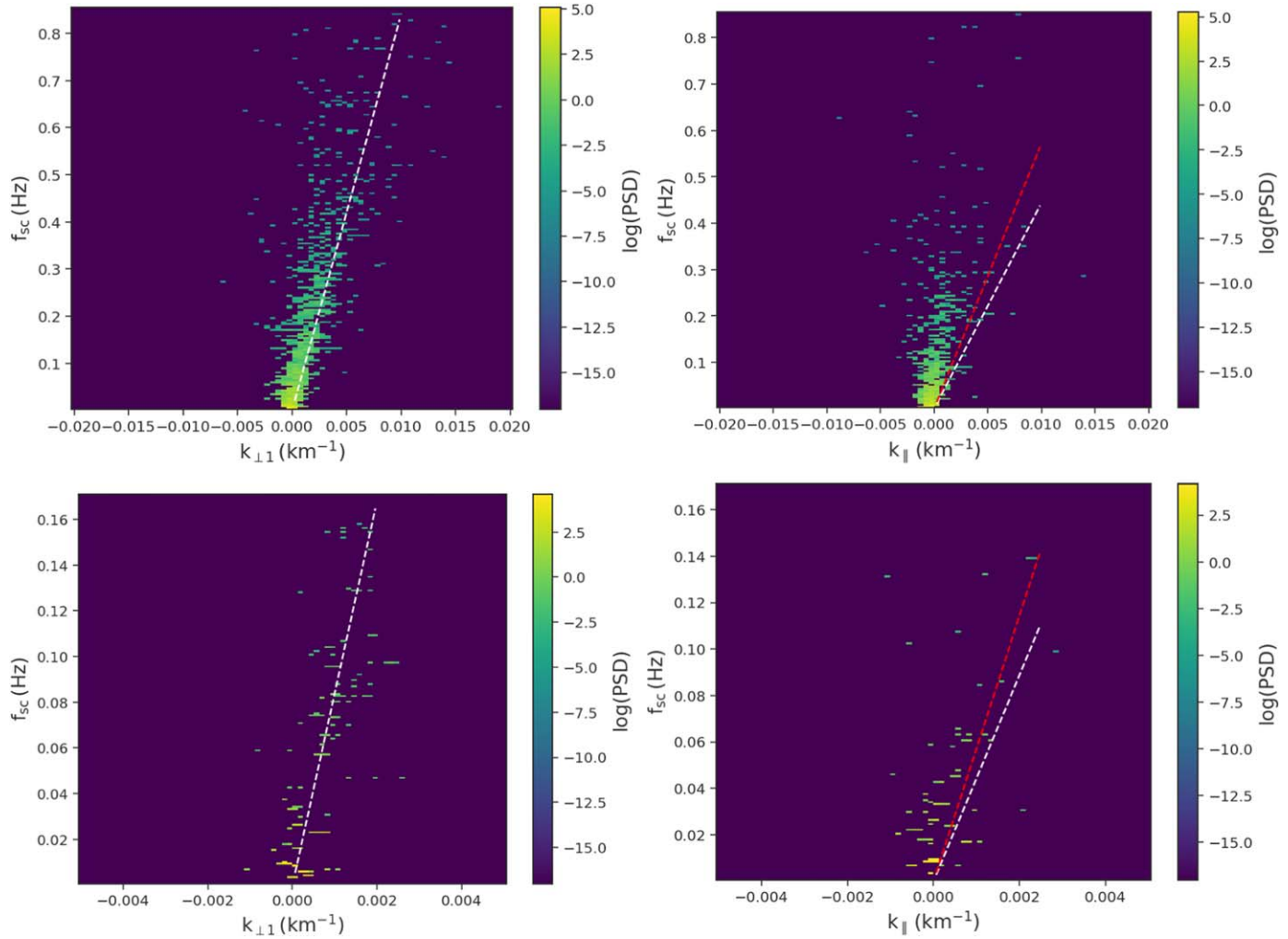

Figure 5. Frequency–wavenumber (ω-$\boldsymbol{k}$) power spectrum for the solar wind interval on 2017 December 18 using the phase differencing method for perpendicular $k_{\perp 1}$ (left panels) and parallel $k_{\parallel}$ (right panels) wavenumbers, respectively. The top two panels show the ω–$\boldsymbol{k}$ spectra at larger wavenumbers and frequencies. The bottom two panels show the results for the smaller wavenumbers. The dashed lines in the left and right panels denote the dispersion relations for nonpropagating structures and propagating Alfvén waves during this interval.

while in the bottom two panels we choose smaller wavenumbers and frequencies to check if propagating Alfvén waves can be seen at smaller wavenumbers, as suggested by Zhao et al. (2022). The results for larger wavenumbers are similar to those from the other interval shown in Figure 3. The fluctuation power in the ω-$k_{\perp 1}$ spectrum shown in the left panel primarily follows the dispersion relation for nonpropagating modes $\omega = \boldsymbol{k} \cdot \boldsymbol{V}_{\rm sw}$. The top right panel shows again that the power in the ω-$k_{\parallel}$ spectrum does not follow the Alfvén wave dispersion relation, illustrated by the white and red dashed lines. Since the parallel flow velocity is larger than the Alfvén speed (i.e., $V_{{\rm sw},z} > V_{\rm A}$) in this interval, both forward and backward propagating Alfvén waves should correspond to the same sign of $k_{\parallel}$. At smaller wavenumbers and frequencies shown in the bottom two panels, the perpendicular ω-$k_{\perp 1}$ spectrum still shows significant evidence of nonpropagating advected structures. In the spectrum of parallel wavenumbers, some fluctuations appear to be present in the region enclosed by the two dispersion relation lines. These may exhibit the characteristics of propagating Alfvén waves. However, this feature is not very prominent compared to the perpendicular wavevector $k_{\perp 1}$ spectrum. The absence of any significant presence of propagating waves during this interval suggests that the conclusion does not depend on the dominant perpendicular flow velocity observed in Interval 1.

For completeness, we provide a rough estimate of the uncertainty of the dispersion relation lines (dashed line in each ω-$\boldsymbol{k}$ spectrum). Based on the dispersion relation $\omega = k_{\parallel} V_{{\rm sw},z} \pm k_{\parallel} V_{\rm A}$, the uncertainty in frequency for the Alfvén waves comes from the parallel flow velocity $V_{{\rm sw},z}$ and $V_{\rm A}$ (provided $k_{\parallel}$ is fixed), and can be crudely estimated as $\delta\omega/\omega_0 \sim \sqrt{(\delta V_{{\rm sw},z}^2 + \delta V_{\rm A}^2)} \big/ \langle V_{{\rm sw},z} + V_{\rm A} \rangle$. Here, we use the plus sign in the dispersion relation. The error is larger if the minus sign is used since $V_{{\rm sw},z}$ and $V_{\rm A}$ have the same sign in both intervals. $\delta V_{{\rm sw},z}$ and $\delta V_{\rm A}$ represent the fluctuation amplitude (calculated by the standard deviation) of the parallel flow speed and the Alfvén speed, respectively. The angle-bracket $\langle ... \rangle$ denotes an ensemble time average over the interval. The resulting uncertainties in frequency for the Alfvén wave dispersion relation lines are about 50% and 30% for Intervals 1 and 2, respectively. Similarly, for nonpropagating structures, we estimate the uncertainty in frequency as $\delta\omega/\omega_0 \sim \delta V_{{\rm sw},\perp} / \langle V_{{\rm sw},\perp} \rangle$ according to its dispersion relation $\omega = k_{\perp} V_{{\rm sw},\perp}$, where $V_{{\rm sw},\perp}$ is the perpendicular flow velocity and $\delta V_{{\rm sw},\perp}$ represents its fluctuation amplitude. The resulting

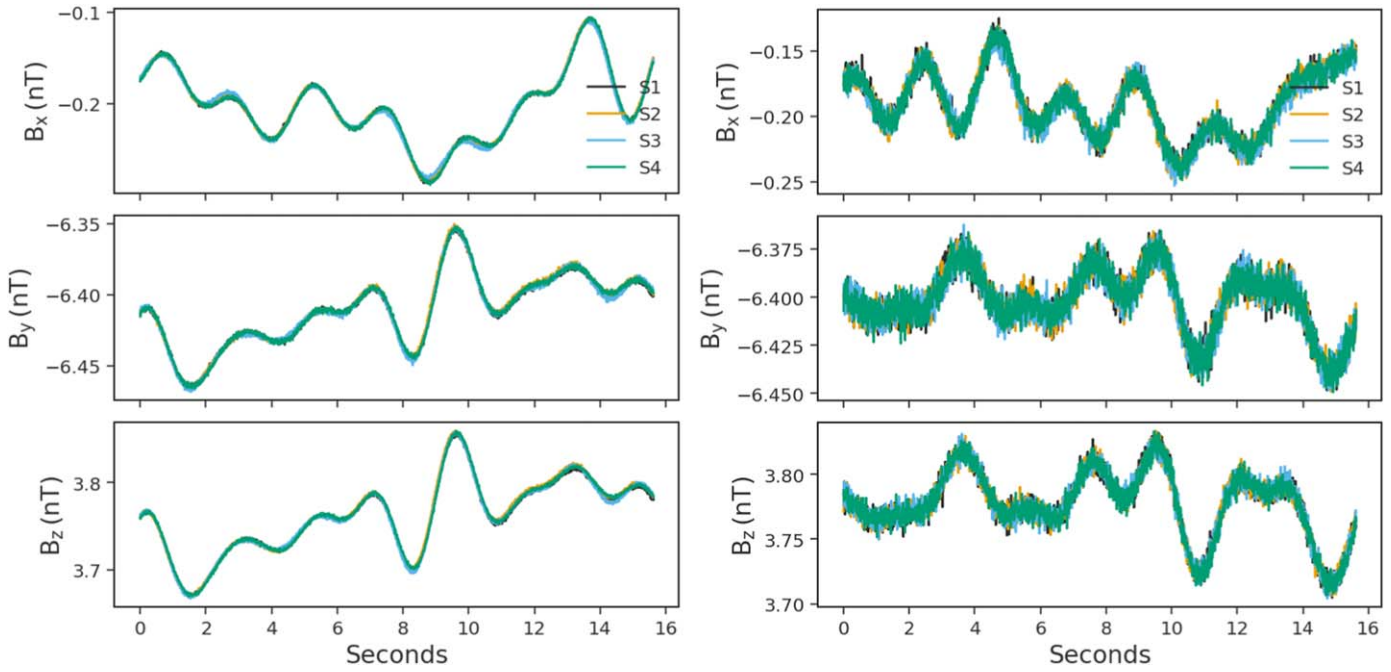

Figure 6. Magnetic field vector synthesized from test waves at four MMS spacecraft locations. The left panel shows synthetic data with lower noise levels, and the right panel shows synthetic data with higher noise levels.

uncertainties in frequency for nonpropagating structure dispersion relation lines are around 1.6% and 9.4% for Intervals 1 and 2, respectively.

4. Synthetic Data Test

To ensure the correctness of our results, we test the analysis technique by using a set of superimposed 100 random 2D nonpropagating modes with $k_{\parallel} = 0$, $\omega = 0$ and 100 Alfvén modes with $k_{\perp} = 0$, $\omega = \pm k_{\parallel} V_{\rm A}$. The mean magnetic field, velocity vector, Alfvén speed, and the location of the four spacecraft are taken from the original MMS measurements in Interval 1. The magnetic fluctuation amplitude of each injected mode is chosen randomly, as is the wavevector and phase of each mode. The propagation direction (determined by the sign of $k_{\parallel}$) of each Alfvén mode is also random. The magnitude of each wavevector component is smaller than 0.1. Figure 6 shows an example of the first 2000 points of the synthetic magnetic field data (from a total of 300,000 points) at each spacecraft location. Two cases with lower and higher noise levels are tested, as shown in the left and right panels, and the differences will be discussed.

The frequency–wavenumber power spectra for the synthetic data with a lower noise level are shown in Figure 7. The top two panels show the frequency–wavenumber spectra using the phase differencing method, and the bottom two panels show the spectra using the k-filtering method. It can be seen that the spectral power follows the expected dispersion curves as indicated by the red dashed lines in each panel. For example, in the $f_{\rm sc} - k_{\perp 1}$ spectra (left panels), the red dashed lines represent $2\pi f_{\rm sc} = k_{\perp} V_{\perp 1}$ with $V_{\perp 1}$ being the solar wind speed along the x-direction in the mean-field coordinates. In the $f_{\rm sc} - k_{\parallel}$ spectra (right panels), the red dashed lines represent $2\pi f_{\rm sc} = k_{\parallel}(V_{\parallel} \pm V_{\rm A})$ with $V_{\parallel}$ being the solar wind speed along the mean-field z direction.

We note in particular that counterpropagating Alfvén waves are clearly visible in the right panels for both methods, suggesting that the absence of Alfvén waves in the observations shown in Figures 3 and 5 is not due to defects of the methodology. On the other hand, the observed $k_{\perp 1}$-spectrum is consistent with the one constructed here from 2D nonpropagating modes.

In fact, the features near $k_{\parallel} = 0$ in Figures 3 and 5 may be explained by instrument noise. Random noise leads to fluctuations observed at all frequencies. This is demonstrated in Figure 8 where we inject higher amplitude uncorrelated Gaussian random numbers into the test data for all four spacecraft as shown in the right panel of Figure 6 and use the phase differencing method. Figure 8 shows that the $k_{\perp}$ spectrum still follows the expected dispersion relation for 2D nonpropagating modes, although somewhat broadened in wavenumber. Interestingly, here the $k_{\parallel}$ spectrum shows similar features to the observed results. Therefore, our results suggest that if Alfvén waves do exist in the observation intervals, their amplitude must be smaller than the noise level indicating that they cannot be observed. We note that the average amplitude of the injected Alfvén modes here is about 1% of that of the injected 2D advected modes. The exact nature of the noise is beyond the scope of this work, but it may be due to instrument uncertainties in spacecraft locations and timing.

5. Conclusions

In this paper, we present an analysis of the magnetic fluctuation frequency–wavenumber spectrum based on MMS measurements using both k-filtering and phase differencing methods. Two solar wind intervals with different speeds and angles between the solar wind velocity and the mean magnetic field are selected for the analysis. The three main conclusions are as follows.

1. The ω-$k_{\perp}$ spectrum shows the presence of quasi-2D structures that are advected and nonpropagating. This is

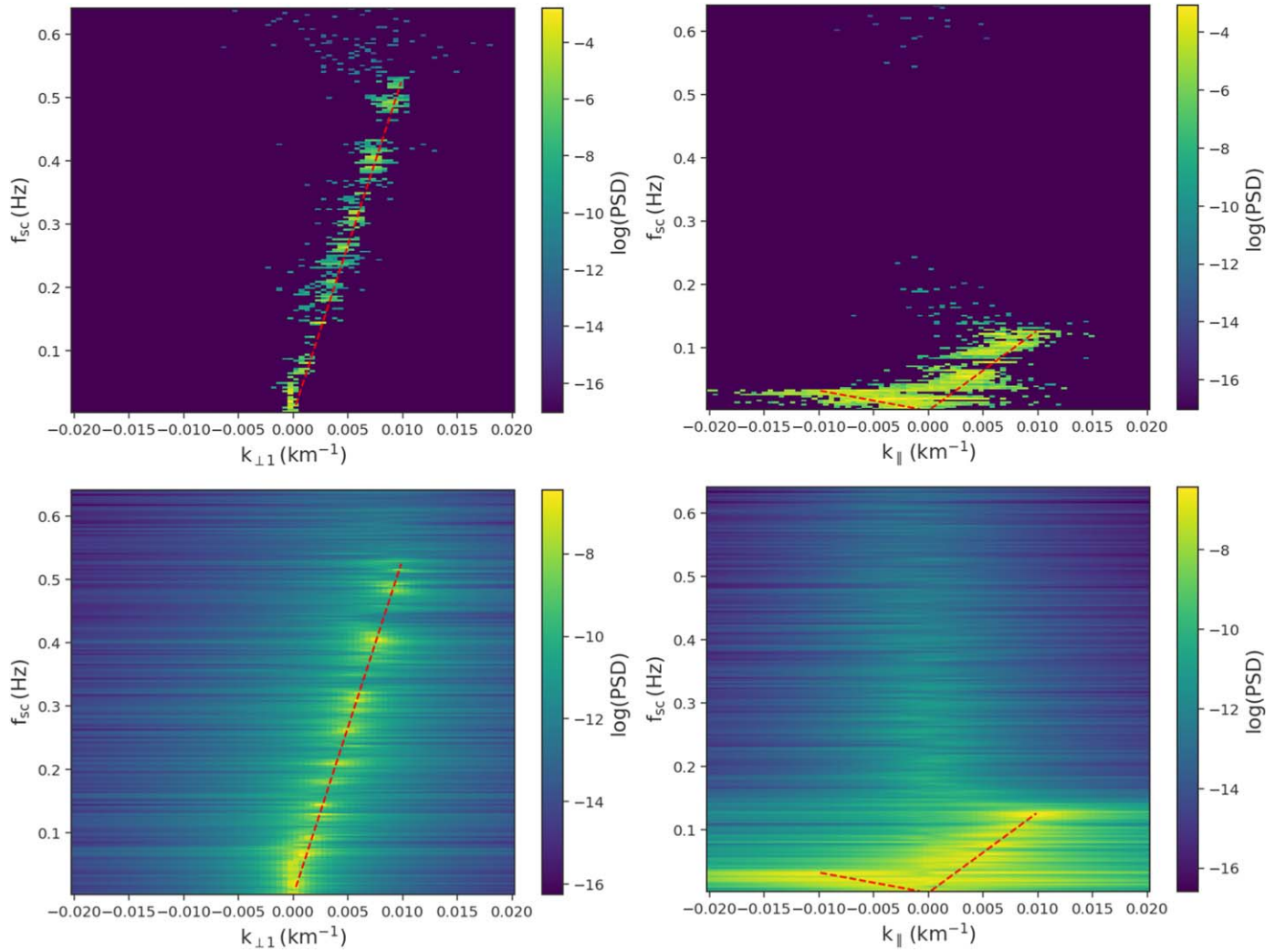

Figure 7. Frequency–wavenumber spectrum with test waves and low noise level using the phase differencing method (top panels) and the *k*-filtering method (bottom panels), respectively. The red dashed lines indicate the expected dispersion relation in the plasma rest frame for the synthetic nonpropagating modes (left panels) and the Alfvén modes (right panels).

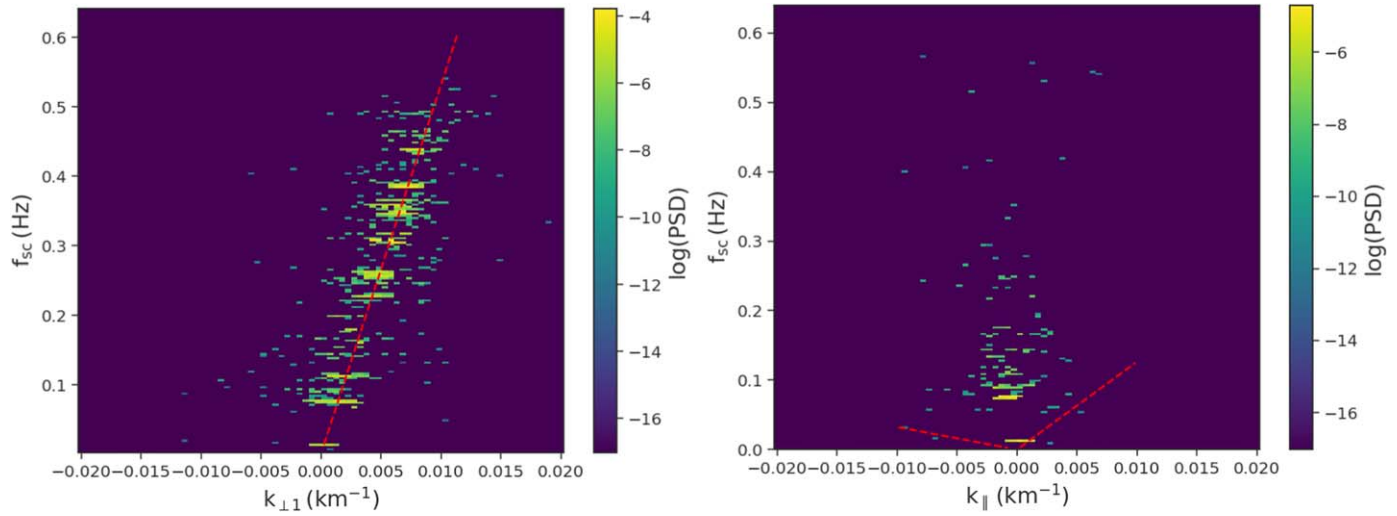

Figure 8. Frequency–wavenumber spectrum of high noise synthetic data using the phase differencing method to show the effects of noise on perpendicular (left panel) and parallel (right panel) fluctuations, respectively.

demonstrated by the fluctuation power that follows $\omega = \boldsymbol{k} \cdot \boldsymbol{V}_{\rm sw}$ associated with $k_\parallel = 0$.
2. The $k_\perp^{-5/3}$ Kolmogorov-like scaling in the inertial range is consistent with magnetized turbulence that is dominated by nonlinear interactions of the advected 2D structures, and therefore, the nonlinear timescale rather than the Alfvén timescale dominates and determines the nature of the cascade process, as suggested by Zank et al. (2017, 2020).
3. There is no clear evidence from the ω-$k_\parallel$ spectrum that shows Alfvén waves (or any other waves) propagating parallel to the mean magnetic field. Furthermore, we show that the observed spectrum is similar to that of noise, suggesting that if parallel propagating waves exist, their amplitudes are smaller than the noise level.

The length scales that we consider are mainly at the small-scale end of the MHD inertial range, and part of the ion kinetic range is also included. The identification of nonpropagating structures appears to be consistent with some recent simulations, such as that by Gan et al. (2022). Nonpropagating structures are also consistent with the view of solar wind turbulence that is dominated by quasi-2D nonlinear structures (e.g., Zank & Matthaeus 1993; Zank et al. 2017). The view has been supported by single-spacecraft evidence (Bieber et al. 1996), but has not explicitly shown with direct measurements by multiple spacecraft. The lack of Alfvén or other parallel propagating waves from MMS measurements at 1 au suggests that linear waves may play a relatively minor role in solar wind turbulence. Our conclusions are in contrast to the recent work by Zhao et al. (2022), which shows the presence of Alfvén waves in the $k_\perp = 0$ dispersion relation. We note that the wavenumbers reported in Zhao et al. (2022) are much smaller than those shown here, and lie in a region dominated by noise in our analysis.

It is well known that the limit of the wavenumber for reliable k-filtering depends on spacecraft separation. Specifically, the average separation of the spacecraft $d_{\rm av}$ in the two intervals considered here is about 16 km and 24 km, respectively. The corresponding limit of the wavenumber is $k_{\rm max} = \pi/d_{\rm av} \simeq 0.2\,{\rm km}^{-1}$ for Interval 1 and $0.13\,{\rm km}^{-1}$ for Interval 2. The range of wavenumber k considered in our analysis falls mostly between the empirical $k_{\rm min}$ (which is about $0.01\,k_{\rm max}$) and $k_{\rm max}$. Since we focus on the inertial range of turbulence, the lower limit of the wavenumber used in this work is smaller than $0.01\,k_{\rm max}$. As suggested by Sahraoui et al. (2010b), the error increases significantly for wavenumbers near and below $0.01\,k_{\rm max}$, so our analysis presented here is pushing the limit of the technique. However, Figure 4 provides some reassurance that the analysis is likely valid even below $0.01\,k_{\rm max}$. In any case, the very small k could be a possible source for the noise that is present in the $k_\parallel$ spectrum, and we do not rule out the possibility that propagating waves can exist in the small-$k_\parallel$ regime. Nevertheless, our analysis reveals clearly that nonpropagating (i.e., $k_\parallel \simeq 0$) fluctuations are a major component in solar wind turbulence. Similar results are also seen by Sahraoui et al. (2010b), where kinetic Alfvén waves are found in the solar wind at the subproton scale using the ω–$k_\perp$ dispersion relation, and the rest-frame frequency, in this case, is also close to zero at scales larger than the proton gyroradius.

We thank the anonymous referee for the thoughtful comments that greatly improved the manuscript. We acknowledge the partial support of the NSF EPSCoR RII-Track-1 Cooperative Agreement OIA-2148653 and NASA awards 80NSSC20K1783 and 80NSSC23K0415. L.Z. is also supported by the ORAU Ralph E. Powe Award. We thank Jiansen He and Rong Lin at Peking University for very helpful discussions on the k-filtering technique. We thank the instruments team of the MMS spacecraft for providing the data. All MMS data used in this study are publicly available at the MMS Science Data Center (https://lasp.colorado.edu/MMS/sdc/public/).

ORCID iDs

L.-L. Zhao https://orcid.org/0000-0002-4299-0490
G. P. Zank https://orcid.org/0000-0002-4642-6192
M. Nakanotani https://orcid.org/0000-0002-7203-0730
L. Adhikari https://orcid.org/0000-0003-1549-5256

References

Balikhin, M. A., Pokhotelov, O. A., Walker, S. N., et al. 2003, GeoRL, 30, 1508
Bandyopadhyay, R., Chasapis, A., Chhiber, R., et al. 2018, ApJ, 866, 81
Belcher, J. W., & Davis, L. 1971, JGR, 76, 3534
Bieber, J. W., Wanner, W., & Matthaeus, W. H. 1996, JGR, 101, 2511
Chaston, C. C., Bonnell, J. W., Bale, S. D., et al. 2020, ApJS, 246, 71
Chisham, G., Burgess, D., Schwartz, S. J., & Dunlop, M. W. 1998, JGR, 103, 26765
Cho, J., & Lazarian, A. 2003, MNRAS, 345, 325
Efthymiadis, D., Jones, P. D., Briffa, K. R., Bohm, R., & Maugeri, M. 2007, JGRD, 112, D12104
Farris, M. H., & Russell, C. T. 1994, JGR, 99, 17681
Gan, Z., Li, H., Fu, X., & Du, S. 2022, ApJ, 926, 222
Glassmeier, K., Motschmann, U., & Stein, R. 1995, AnGeo, 13, 76
He, J., Zhu, X., Verscharen, D., et al. 2020, ApJ, 898, 43
King, J. H., & Papitashvili, N. E. 2005, JGRA, 110, A02104
Lin, R., He, J., Zhu, X., et al. 2022, ApJ, 939, 121
Matthaeus, W. H., Goldstein, M. L., & Roberts, D. A. 1990, JGR, 95, 20673
Matthaeus, W. H., Weygand, J. M., & Dasso, S. 2016, PhRvL, 116, 245101
Motschmann, U., Woodward, T. I., Glassmeier, K. H., Southwood, D. J., & Pincon, J. L. 1996, JGR, 101, 4961
Narita, Y., Glassmeier, K.-H., Sahraoui, F., & Goldstein, M. L. 2010, PhRvL, 104, 171101
Narita, Y., Plaschke, F., Nakamura, R., et al. 2016, GeoRL, 43, 4774
Pincon, J. L., & Lefeuvre, F. 1988, AdSpR, 8, 459
Pinçon, J.-L., & Motschmann, U. 1998, Multi-Spacecraft Filtering: General Framework, ESA/ISSI, 65
Podesta, J. J. 2009, ApJ, 698, 986
Pollock, C., Moore, T., Jacques, A., et al. 2016, SSRv, 199, 331
Roberts, O. W., Nakamura, R., Torkar, K., et al. 2020, ApJS, 250, 35
Roberts, O. W., Narita, Y., Nakamura, R., Vörös, Z., & Gershman, D. 2019, FrP, 7, 184
Russell, C. T., Anderson, B. J., Baumjohann, W., et al. 2016, SSRv, 199, 189
Sahraoui, F., Belmont, G., Goldstein, M. L., & Rezeau, L. 2010a, JGRA, 115, A04206
Sahraoui, F., Belmont, G., Rezeau, L., et al. 2006, PhRvL, 96, 075002
Sahraoui, F., Goldstein, M. L., Belmont, G., Canu, P., & Rezeau, L. 2010b, PhRvL, 105, 131101
Shue, J.-H., Song, P., Russell, C. T., et al. 1998, JGR, 103, 17691
Tjulin, A., Pincon, J.-L., Sahraoui, F., Andre, M., & Cornilleau-Wehrlin, N. 2005, JGRA, 110, A11224
Walker, S. N., Sahraoui, F., Balikhin, M. A., et al. 2004, AnGeo, 22, 3021
Zank, G. P., Adhikari, L., Hunana, P., et al. 2017, ApJ, 835, 147
Zank, G. P., & Matthaeus, W. H. 1993, PhFlA, 5, 257
Zank, G. P., Nakanotani, M., Zhao, L.-L., Adhikari, L., & Telloni, D. 2020, ApJ, 900, 115
Zhao, L.-L., Zank, G. P., Adhikari, L., et al. 2022, ApJL, 934, L36
Zhao, L.-L., Zank, G. P., He, J. S., et al. 2021, ApJ, 922, 188
Zhao, S. Q., Yan, H., Liu, T. Z., Liu, M., & Wang, H. 2022, ApJ, 937, 102
Zhu, X., He, J., Verscharen, D., Duan, D., & Bale, S. D. 2020, ApJL, 901, L3